International Journal of Microwave and Wireless Technologies

cambridge.org/mrf

A compact corrugated double-tapered slot Vivaldi antenna with resonator-based interference suppression and AZIM-enhanced gain

Manoj Bhaskar[1,2], Chetan Barde[1], Prakash Ranjan[1], Sujit Kumar[3], Himanshu Kumar Shekhar[2,4] and Bam Bahadur Sinha[5]

[1]Department of Electronics and Communication Engineering, Indian Institute of Information Technology Bhagalpur, Bhagalpur, Bihar, India; [2]Department of Electronics and Communication Engineering, Government Engineering College, Science, Technology and Technical Education Department, Bihar Engineering University, Banka, India; [3]Department of Electrical Engineering, Government Engineering College Banka, Science, Technology and Technical Education Department, Bihar Engineering University, Banka, India; [4]Department of Electronics and Communication Engineering, Indian Institute of Technology Roorkee, Roorkee, Uttarakhand, India and [5]Department of Computer Science and Engineering, National Institute of Technology Sikkim, Ravangla, Sikkim, India

Research Paper

Cite this article: Bhaskar M, Barde C, Ranjan P, Kumar S, Shekhar HK, Sinha BB (2026) A compact corrugated double-tapered slot Vivaldi antenna with resonator-based interference suppression and AZIM-enhanced gain. *International Journal of Microwave and Wireless Technologies* **18**(5), 811–826. https://doi.org/10.1017/S1759078726103353

Received: 23 January 2026
Revised: 6 May 2026
Accepted: 8 May 2026
First published online: 28 May 2026

Keywords:
AZIM; Corrugation; CSRR; DTSVA; EMI; Gain Enhancement; Triple Band-Notched

Corresponding author: Manoj Bhaskar; Email: manoj.bhaskar.89@gmail.com

Abstract

This paper presents the design and experimental validation of a compact corrugated double-tapered slot Vivaldi antenna (DTSVA) for ultra-wideband (UWB) applications. The proposed antenna provides efficient impedance matching over a wide frequency range of 1–20 GHz. To suppress electromagnetic interference from coexisting narrowband systems, triple band-notched characteristics are realized using spatially distributed resonant elements, including a complementary split-ring resonator (CSRR) and U-shaped slots etched beneath different sections of the feed network, enabling effective rejection of WiMAX (3.3–3.8 GHz), WLAN (5.15–5.85 GHz), and X-band uplink (7.9–8.4 GHz) signals. To enhance forward radiation without increasing the antenna size, corrugated edges and an anisotropic zero-index metamaterial (AZIM) unit cell are integrated within the tapered slot region. Consequently, the proposed antenna achieves a maximum peak realized gain of 12.5 dBi, corresponding to an improvement of up to 3.8 dBi compared to the reference DTSVA. Simulated and measured results show good agreement in terms of impedance bandwidth, radiation characteristics, realized gain, and group delay. Owing to its compact size, enhanced gain, stable time-domain performance, and effective interference suppression, the proposed antenna is well suited for portable indoor and outdoor UWB applications, including imaging, radar sensing, and material characterization.

Introduction

Ultra-wideband (UWB) antennas have attracted significant attention due to their capability to support high data rates, fine spatial resolution, and reliable performance over a wide frequency spectrum. Among various UWB radiators, Vivaldi antennas are particularly attractive owing to end-fire radiation characteristics, broad impedance bandwidth, stable radiation patterns, and planar configuration.

As a result, such systems have been widely employed in applications such as microwave imaging, non-destructive testing (NDT), ground-penetrating radar, through-wall imaging, satellite communications, and emerging wireless systems [1–5].

The Vivaldi antenna was originally introduced by Gibson as a coplanar tapered slot antenna [6]. Subsequent developments led to the antipodal Vivaldi antenna (AVA), which offers improved impedance bandwidth and gain performance [7]. AVAs generally exhibit higher cross-polarization levels and larger electrical dimensions compared to conventional tapered slot Vivaldi antennas (TSVAs), which limits the suitability for compact and portable systems [8, 9]. In imaging and NDT applications, antenna performance is strongly influenced by operating frequency, as lower frequencies provide deeper penetration in lossy media, whereas higher frequencies offer improved spatial resolution. This trade-off necessitates antennas with UWB operation and stable radiation characteristics across a wide frequency range [10–12]. A key challenge associated with UWB antennas is electromagnetic (EM) interference from coexisting narrowband wireless systems, such as IEEE 802.16 WiMAX (3.3–3.8 GHz), IEEE 802.11 WLAN

© The Author(s), 2026. Published by Cambridge University Press in association with The European Microwave Association.

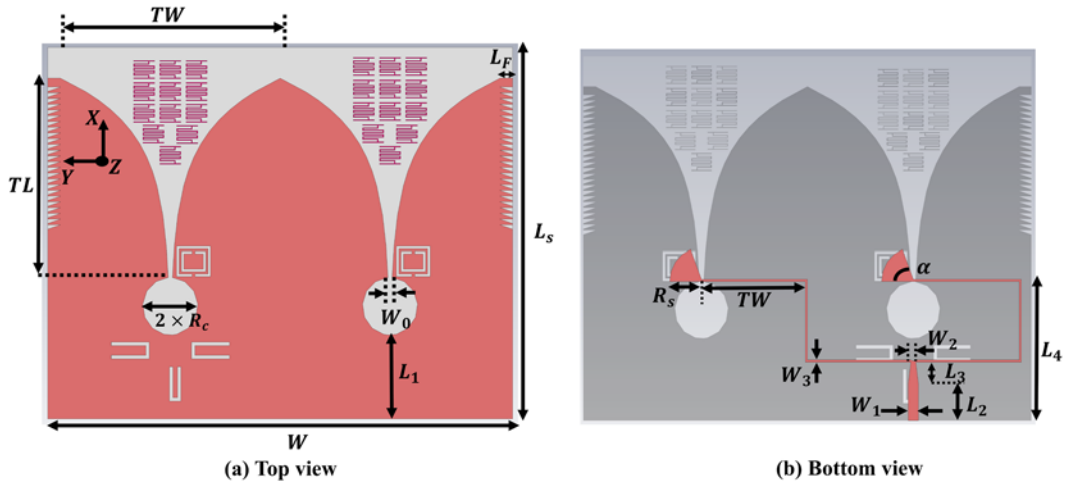


Figure 1. Geometry of the proposed corrugated DTSVA: (a) top view showing the tapered slot, corrugations, loading resonator, and AZIM unit-cell elements; and (b) bottom view illustrating the microstrip feed configuration with key dimensions.

(5.15–5.85 GHz), and X-band satellite uplinks (7.9–8.4 GHz). Such interference can significantly degrade system performance and imaging accuracy. Conventional mitigation approaches based on external band-stop filters increase system complexity, insertion loss, and overall size. Consequently, antenna-integrated band-notched techniques have been extensively investigated, including the incorporation of slots, parasitic elements, and resonant structures within the radiating or ground planes [13–22]. Various resonator-based approaches employing split-ring resonators (SRRs), complementary SRRs (CSRRs), stepped-impedance resonators, and slot configurations have been reported to achieve single-, dual-, and multi-band rejection [23–26].

In addition to interference suppression, gain enhancement remains a critical issue for compact Vivaldi antennas, particularly at lower frequencies. Several techniques, including edge corrugations [27], tapered slot profile optimization [28], aperture shaping [29], and parasitic element loading [30], have been proposed to improve radiation performance. Although dielectric lenses and metamaterial-based superstructures can significantly enhance gain, such structures often increase antenna size and structural complexity, thereby limiting applicability in portable imaging and NDT systems [31, 32, 33]. More recently, metamaterial integration has emerged as an effective approach for compact gain enhancement. Zero-index metamaterials (ZIMs) and epsilon-near-zero structures improve end-fire radiation by enabling controlled wave propagation and field collimation [34–36, 39, 40, 53]. In particular, anisotropic zero-index metamaterials (AZIMs) provide additional degrees of freedom for tailoring EM responses, allowing gain enhancement without increasing antenna dimensions [37, 38]. Nevertheless, compact TSVAs operating over an ultra-wide frequency range extending down to 1 GHz while maintaining high directivity and stable radiation characteristics remain relatively unexplored.

Motivated by the above challenges, this paper proposes a compact corrugated double-tapered slot Vivaldi antenna (DTSVA) integrated with spatially distributed resonant elements and AZIM loading. The proposed antenna is fabricated on a low-cost FR-4 substrate ($\varepsilon_r = 4.3$, $\tan\delta = 0.025$) with overall dimensions of $110 \times 84 \times 0.8$ mm^3 and achieves UWB operation from 1 to 20 GHz with triple band-notched characteristics to suppress interference from WiMAX, WLAN, and X-band satellite communication systems. Furthermore, corrugation and AZIM loading are employed to enhance antenna gain while preserving compact size and stable radiation behavior, making the proposed design well-suited for portable microwave imaging and NDT applications.

Proposed antenna design and configuration

The proposed methodology follows a systematic design optimization validation framework for the development of a compact corrugated DTSVA fabricated on a low-cost FR-4 substrate.

The layout of the proposed antenna is illustrated in Figure 1. The overall structure is oriented in the x–y plane, with the feeding network implemented on the back side of the substrate to facilitate compact integration. The antenna is based on a double exponential tapered slot geometry characterized by a tapered length TL and a tapered width TW. The impedance profile of the tapered slot aperture follows the classical exponential formulation for tapered slot antennas [6], and is given by Equation 1

$$y = Ae^{mx} - \left(-\frac{W_o}{2} + A\right), \tag{1}$$

where "m" is computed using Equation 2.

$$m = \frac{1}{TL} \ln\left(\frac{TW/2 - (W_o/2 - A)}{A}\right), \tag{2}$$

constant $A = 0.55$, W_o is the initial slotline width according to 100 Ω. To enhance radiation characteristics and improve impedance matching, a circular aperture of diameter $2R_c$ is introduced at the center of the tapered slot.

The antenna is excited through a microstrip feed line consisting of two cascaded sections corresponding to 50 and 100 Ω transmission lines. A radial stub with radius R_s and flare angle $\alpha = 70^\circ$ is employed to realize a smooth transition from the unbalanced microstrip line to the balanced slot line, thereby functioning as a wideband balun. To achieve triple band-notched characteristics, several resonant elements are incorporated on the top surface of the substrate. Each resonator is electromagnetically coupled to a different current path, enabling independent notch tuning. A CSRR etched beneath the radial stub suppresses the IEEE 802.16 WiMAX band (3.3–3.8 GHz). A pair of horizontally oriented U-shaped slots located below the 100 Ω feed line rejects the IEEE 802.11 WLAN

https://doi.org/10.1017/S1759078726103353 Published online by Cambridge University Press

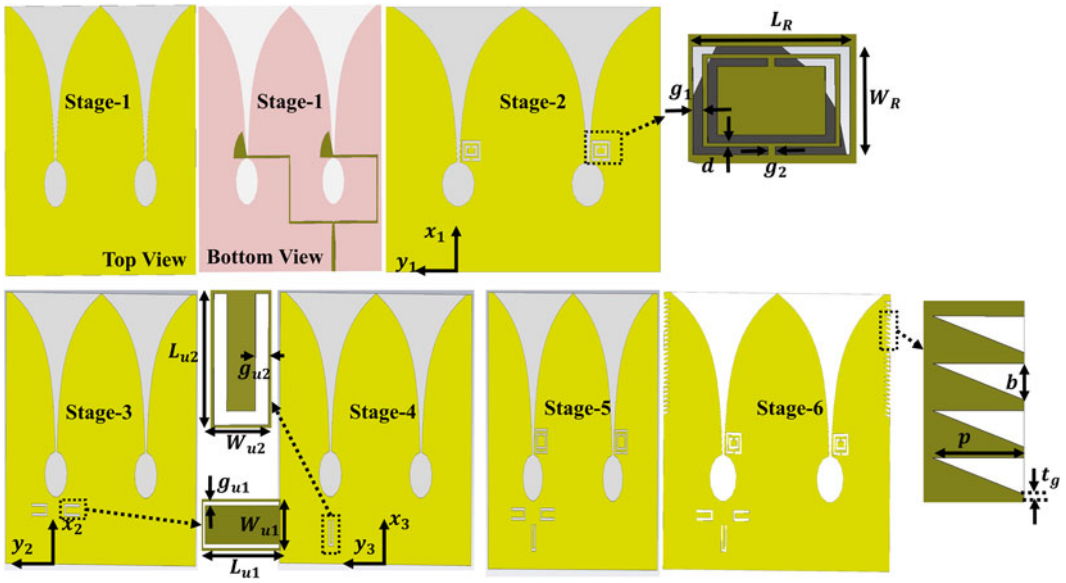


Figure 2. Evolution of the proposed antenna geometry through six design stages. Stage 1 shows the reference antenna (top and bottom views), Stage 2 introduces the CSRR for band rejection, Stage 3 and Stage 4 incorporate horizontal and vertical U-shaped slots, Stage 5 combines multiple notching elements, and Stage 6 further integrates triangular slit corrugations. Insets illustrate the detailed geometrical parameters of the CSRR, U-slots, and corrugation profile.

band (5.15–5.85 GHz), while a vertically oriented U-slot positioned beneath the 50 Ω line near the input port suppresses the X-band satellite uplink band (7.9–8.4 GHz).

In addition, triangular corrugations are introduced along the tapered edges to enhance radiation performance at lower frequencies. An AZIM unit cell is embedded between the tapered arms to improve the peak realized gain without increasing the antenna size. While the AZIM loading primarily enhances gain above 4 GHz, the triangular corrugation significantly improves performance in the 1–3 GHz range. The combined design features result in a compact, high-performance UWB antenna with selective interference suppression, making it well suited for microwave imaging and NDT applications.

Triple-band notch DTSVA design: geometrical parameters and location of loaded resonators analysis

To achieve selective suppression of narrowband interferences within the UWB spectrum while maintaining good impedance matching, a progressive and systematic design methodology is adopted. The design evolution, illustrated in Figure 2 (Stages 1–6), demonstrates the step-by-step incorporation of resonant elements and structural modifications to realize triple band-notched characteristics along with improved radiation performance.

Stage 1 represents the reference configuration corresponding to the basic DTSVA without any notching elements. This configuration provides stable UWB impedance matching over the 1–20 GHz frequency range, as shown in Figure 3, but remains vulnerable to interference from coexisting narrowband wireless systems. To mitigate this issue, a rectangular CSRR is integrated into the radiating surface in Stage 2, as shown in Figure 2.

The CSRR is designed to suppress the IEEE 802.16 WiMAX band (3.3–3.8 GHz). The CSRR geometry is characterized by its outer length L_R, width W_R, outer and inner slot gaps g_1, coupling strip width g_2, and inner strip width d. The resonant frequency

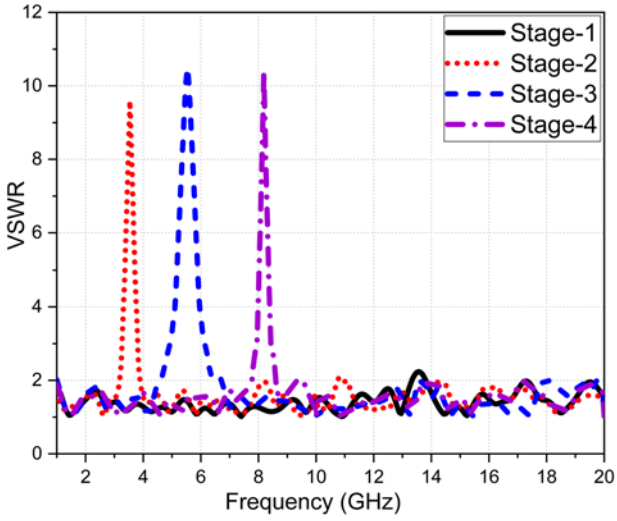


Figure 3. Variation of the simulated VSWR with operating frequency for the four design stages (Stage 1 to Stage 4).

f_1 of the CSRR can be approximately expressed using Equation 3 [41, 42].

$$f_1 = \sqrt{\frac{1}{2\pi^3 r_o L_o C}}, \tag{3}$$

where L_o denotes the inductance per unit length between the annular slots, C is the total capacitance of the resonator, and r_o is the mean radius of the CSRR. Although no closed-form expression directly correlates the CSRR dimensions with its resonant frequency, increasing the overall resonator size generally shifts the notched band toward lower frequencies. Using CST Microwave Studio (CST-MWS), the CSRR dimensions are optimized to L_R = 6.4 mm, W_R = 5.5 mm, g_1 = 0.4 mm, and g_2 = d = 0.2 mm,

https://doi.org/10.1017/S1759078726103353 Published online by Cambridge University Press

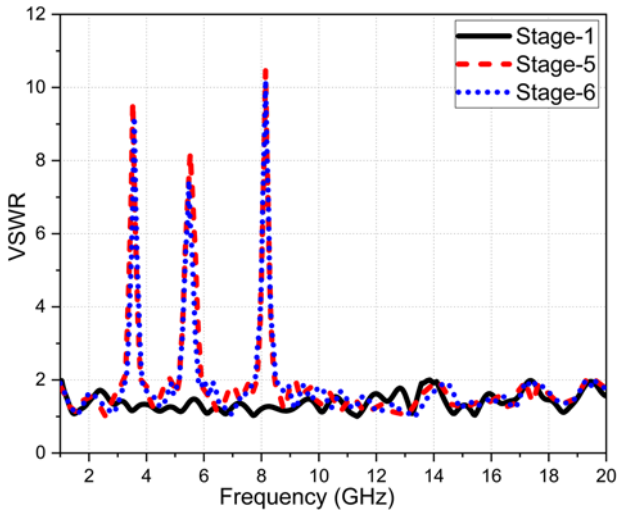


Figure 4. Variation of the simulated VSWR with operating frequency for Stage 1, Stage 5, and Stage 6 antenna configurations.

resulting in a sharp rejection band centered at 3.55 GHz.To generate the second and third notched bands corresponding to the IEEE 802.11 WLAN band (5.15–5.85 GHz) and the X-band satellite uplink (7.9–8.4 GHz), U-shaped slot resonators are incorporated into the antenna structure. As illustrated in Stage 3, a pair of horizontal U-shaped slots is etched beneath the 100 Ω transmission line, while a vertically oriented U-shaped slot is positioned beneath the 50 Ω feed line near the input port in Stage 4. The design of the U-shaped slots follows the condition that the effective slot perimeter is approximately equal to half of the guided wavelength at the desired notch frequency, given by Equation 4.

$$P_{u1} = \frac{c}{2f_2\sqrt{\varepsilon_{\text{eff}}}}, \quad P_{u2} = \frac{c}{2f_3\sqrt{\varepsilon_{\text{eff}}}}, \tag{4}$$

where P_{u1} and P_{u2} represent the effective perimeters of the horizontal and vertical U-slots, respectively. The perimeters are defined via Equations 5 and 6.

$$P_{u1} = 2(L_{u1} - g_{u1}) + (W_{u1} - 2g_{u1}), \tag{5}$$

$$P_{u2} = 2(L_{u2} - g_{u2}) + (W_{u2} - 2g_{u2}). \tag{6}$$

The effective dielectric constant ε_{eff} is estimated using Equation 7 [43].

$$\varepsilon_{\text{eff}} = \frac{\varepsilon_r + 1}{2} + \frac{\varepsilon_r - 1}{2}\left(1 + \frac{12H_s}{W_m}\right)^{-1/2}, \tag{7}$$

where ε_r is the relative permittivity of the substrate, H_s is the substrate thickness, and W_m is the microstrip line width. Based on these relations, the effective perimeters required to realize notches at 5.5 and 8.15 GHz are approximately 15 and 11 mm, respectively, g_{u1} and g_{u2} fixed at 0.3 mm. Accordingly, the initial dimensions are selected as $L_{u1} = 7.8$ mm, $W_{u1} = 2.4$ mm and $L_{u2} = 5.7$ mm, $W_{u2} = 1.2$ mm. Simulation results confirm the formation of two distinct rejection bands at the desired frequencies.

The spatial placement of the resonant elements plays a critical role in controlling the notch behavior. The CSRR is positioned at (x_1, y_1), as shown in Stage 2 of Figure 2, to maximize coupling with the surface current distribution. The horizontal U-slot pair is placed at a distance x_2 beneath the 100 Ω transmission line, while the vertical U-slot is located at a distance y_3 beneath the 50 Ω feed line. Figure 3 illustrates the evolution of the VSWR response through successive design stages. Stage 1 exhibits stable UWB impedance matching, whereas Stage 2 introduces a sharp notch around 3.5 GHz due to the CSRR loading. In Stage 3 and Stage 4, additional notches centered at 5.6 and 8.2 GHz are realized through the horizontal and vertical U-shaped slots, respectively. Outside the rejected bands, all stages maintain VSWR values below 2, confirming preserved UWB performance. Finally, Stage 5 integrates all three resonators, which are strategically positioned to ensure independent operation with minimal mutual coupling, thereby enabling effective triple band-notched behavior without degrading the UWB impedance characteristics. The VSWR responses of Stage 1, Stage 5, and Stage 6 are compared in Figure 4. The VSWR response of Stage 5 clearly demonstrates the formation of three sharp notched bands with minimal mutual coupling among the resonators. After introducing triangular trimming in Stage 6, the VSWR response remains nearly identical to that of Stage 5, indicating that the corrugations do not adversely affect the triple band-notched behavior or the overall UWB impedance matching. Figure 5 illustrates the simulated surface current distributions at the three notched frequencies. At 3.5 GHz, strong current confinement around the CSRR confirms its role in generating the WiMAX rejection band. At 5.6 GHz, intense currents are localized along the horizontal U-shaped slots, validating the WLAN notch mechanism. Similarly, at 8.2 GHz, the current concentration around the vertical U-shaped slot verifies effective suppression of the X-band interference.

Equivalent circuit modeling of Stage 5 DTSVA incorporating three resonators

The equivalent circuit model of the Stage 5 antenna is illustrated in Figure 6. The overall structure comprises a grounded feed line, a resonating network, a UWB section and the substrate. The impedance of the feed line ($Z_{\text{feed_line}}$) is modeled using a series combination of resistance (R_f) and inductance (L_f). The resonating structure is represented by $Z_{\text{resonator}}$, which includes contributions from the horizontal U-slot, vertical U-slot, and CSRR.

The CSRR and U-shaped slots [56, 57] etched in the radiating patch are modeled as series RLC resonators connected in shunt with the feed line and the UWB impedance. Specifically, the vertical U-slot is modeled using (R_1, L_1, C_1), while the paired horizontal U-slot is represented by (R_2, R_3, L_2, L_3, C_2, C_3). Similarly, the paired CSRR structure is modeled using (R_4, R_5, L_4, L_5, C_4, C_5). The UWB behavior of the antenna is characterized by a distributed impedance profile arising from the tapered Vivaldi structure. This behavior is approximated using an equivalent parallel RLC network connected in series with the feed line [54, 55]. To capture the distributed impedance nature of the tapered Vivaldi profile, the equivalent lumped elements are subdivided into multiple parallel RLC sections, represented by R_6, R_7, R_8, L_6, L_7, L_8, and C_6, C_7, C_8. Finally, the substrate effect is modeled using an equivalent impedance (Z_{sub}), represented by resistance (R_9) and capacitance (C_9), accounting for dielectric losses and capacitive coupling.

The input impedance for the equivalent circuit is expressed via Equations 8–16.

$$Z_{\text{input}} = Z_{\text{feed_line}} + (Z_{\text{resonator}} \parallel Z_{\text{UWB}} \parallel Z_{\text{sub}}) \tag{8}$$

where

$$Z_{\text{feed_line}} = R_f + j\omega L_f \tag{9}$$

https://doi.org/10.1017/S1759078726103353 Published online by Cambridge University Press

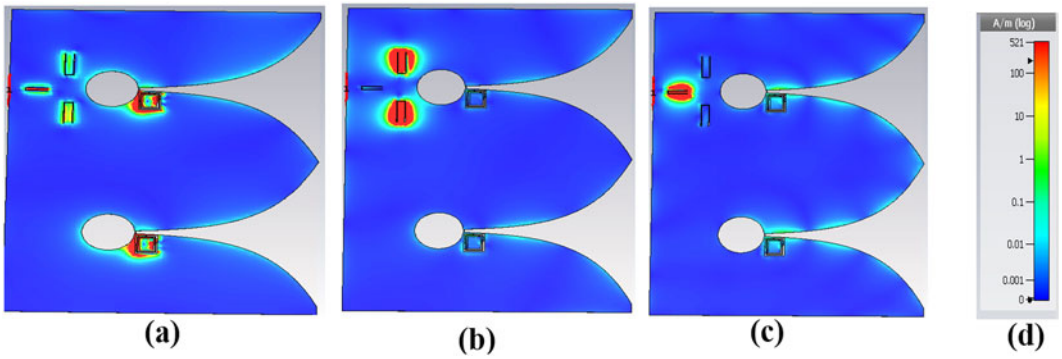


Figure 5. Surface current distribution at (a) 3.5 GHz, (b) 5.6 GHz, and (c) 8.2 GHz with the color scale shown in (d).

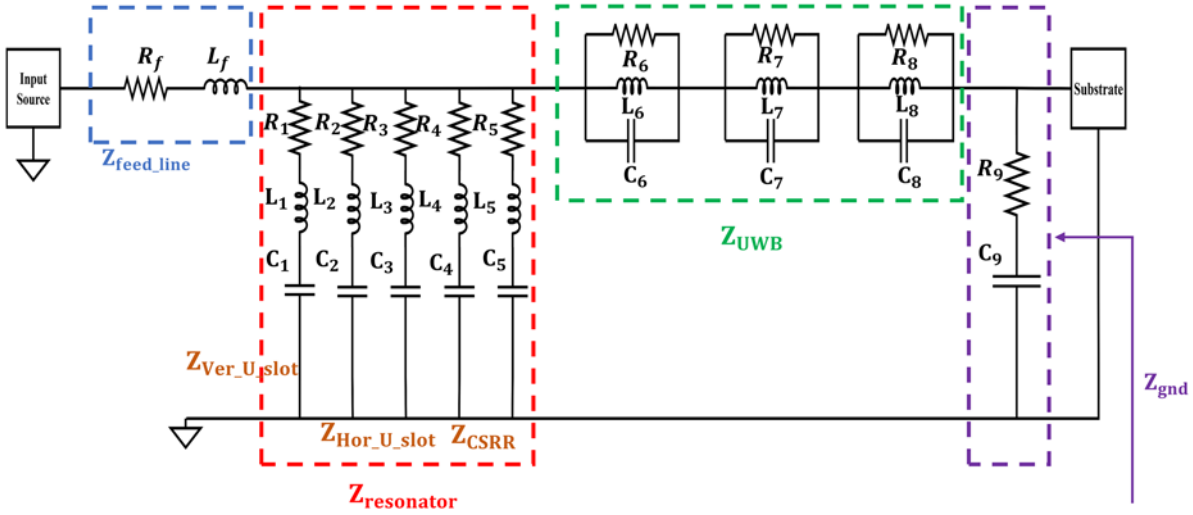


Figure 6. Equivalent circuit model of the DTSVA with three resonators corresponding to Stage 5.

$$Z_{\text{resonator}} = [Z_{\text{Hor_U_Slot}} \parallel Z_{\text{Ver_U_Slot}} \parallel Z_{\text{CSRR}}] \tag{10}$$

$$Z_{\text{Hor_U_Slot}} = R_1 + j\omega L_1 - \frac{j}{\omega C_1} \tag{11}$$

$$Z_{\text{Ver_U_Slot}} = \left[R_2 + j\omega L_2 - \frac{j}{\omega C_2}\right] \parallel \left[R_3 + j\omega L_3 - \frac{j}{\omega C_3}\right] \tag{12}$$

$$Z_{\text{CSRR}} = \left[R_4 + j\omega L_4 - \frac{j}{\omega C_4}\right] \parallel \left[R_5 + j\omega L_5 - \frac{j}{\omega C_5}\right] \tag{13}$$

$$Z_{\text{UWB}} = \sum_{k=6}^{8} \left(\frac{1}{R_k} + \frac{1}{j\omega L_k} + j\omega C_k\right)^{-1} \tag{14}$$

$$Z_{\text{sub}} = R_9 - \frac{j}{\omega C_9} \tag{15}$$

$$Z_{\text{gnd}} = jZ_{\text{sub}} \tan(\beta \cdot \text{thickness}) \tag{16}$$

where $Z_{\text{sub}} = \frac{377}{\sqrt{\varepsilon_r}} = 181.80\,\Omega$ represents the characteristic impedance of the short-circuited transmission line, and $\beta = \frac{\omega\sqrt{\varepsilon_r}}{c} = 0.69 \times 10^{-0.8}\,\omega$ rad/m is the phase constant of the wave in the substrate.

The reflection coefficient is obtained by using Equation 17.

$$S_{11} = \frac{Z_{\text{input}}(\omega) - 50}{Z_{\text{input}}(\omega) + 50} \tag{17}$$

The design is simulated using CST. The obtained S_{11} results are further validated through the equivalent circuit model using the Keysight ADS simulation tool, as illustrated in Figure 6. The extracted passive element values are as follows: $R_f = 50\,\Omega$, $R_1 = 70\,\Omega$, $R_2 = 62\,\Omega$, $R_3 = 73\,\Omega$, $R_4 = 110\,\Omega$, $R_5 = 95\,\Omega$, $R_6 = 60\,\Omega$, $R_7 = 40\,\Omega$, $R_8 = 55\,\Omega$, $R_9 = 100\,\Omega$; $L_f = 0.86\,nH$, $L_1 = 0.8\,nH$, $L_2 = 1.8\,nH$, $L_3 = 1.51\,nH$, $L_4 = 3.5\,\text{nH}$, $L_5 = 2.7\,\text{nH}$, $L_6 = 2.5\,\text{nH}$, $L_7 = 1\,\text{nH}$, $L_8 = 0.25\,\text{nH}$; $C_1 = 0.48\,\text{pF}$, $C_2 = 0.53\,\text{pF}$, $C_3 = 0.48\,\text{pF}$, $C_4 = 0.66\,\text{pF}$, $C_5 = 0.62\,\text{pF}$, $C_6 = 1.12\,\text{pF}$, $C_7 = 1.54\,\text{pF}$, $C_8 = 0.41\,\text{pF}$, and $C_9 = 1.2\,\text{pF}$.

Figure 7 illustrates the comparison of S_{11} obtained from CST simulation and the ADS-based equivalent circuit model. A good agreement between the two results is observed, with minor deviations of approximately $\pm 5\%$ within acceptable tolerance limits.

https://doi.org/10.1017/S1759078726103353 Published online by Cambridge University Press

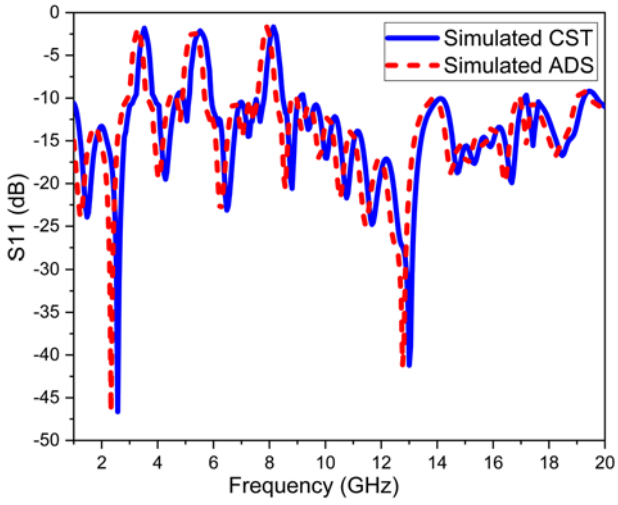


Figure 7. Comparison of simulated S_{11} results of the Stage 5 antenna obtained from CST and ADS.

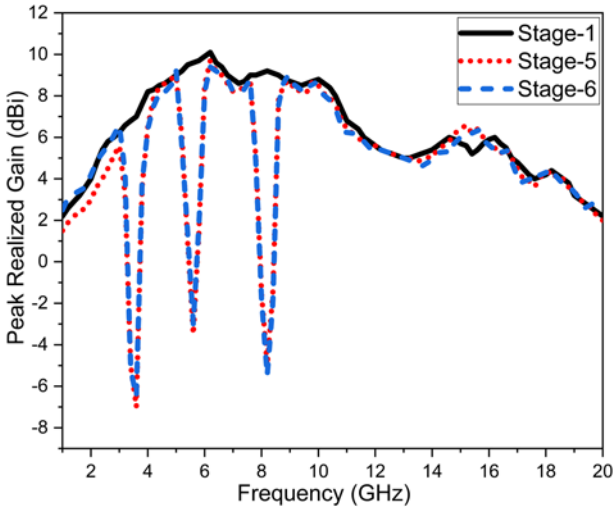


Figure 8. Simulated peak realized gain of the antenna for Stage 1, Stage 5, and Stage 6 configurations over the operating frequency band.

Table 1. Optimized geometrical parameters of the proposed antenna

Parameter	Value (mm)	Parameter	Value (mm)	Parameter	Value (mm)
L_s	84	R_s	6.3	g_{u2}	0.3
L	77	L_R	6.4	x_3	4
W	110	W_R	5.5	y_3	−0.2
T_L	44.9	g_1	0.4	p	3
T_W	52	g_2	0.3	b	1
W_o	1	d	0.2	t_g	0.3
R_c	6.5	x_1	32.5	y_2	5
L_1	16	y_1	1.2	L_{u2}	5.7
L_f	3	L_{u1}	7.8	W_{u2}	1.2
W_1	1.5	W_{u1}	2.4	L_3	8.5
W_2	0.22	g_{u1}	0.3	x_2	13.5
W_3	1.2	L_2	5	L_4	32.2

Effect of triangular trimming in triple-notched DTSVA

To further enhance the peak realized gain in the lower frequency range of 1–3 GHz, triangular corrugations are introduced along the tapered edges of the antenna, as illustrated in Stage 6. The corrugation geometry, defined by the parameters p, b, and t, is carefully optimized to improve end-fire radiation while preserving the impedance characteristics of the triple-notched design. The optimized value of all geometric parameters shown in Figures 1 and 2 are provided in Table 1. The simulated peak realized gain characteristics of Stage 1, Stage 5, and Stage 6 are presented in Figure 8. The reference antenna (Stage 1) exhibits a peak realized gain of approximately 10 dBi. However, the introduction of multiple resonators in Stage 5 results in gain degradation in the 1–3 GHz frequency range due to increased current perturbation and localized field confinement. With the incorporation of triangular corrugations in Stage 6, the realized gain is noticeably improved over the 1–3 GHz band compared to Stage 5, while maintaining a maximum gain of approximately 10 dBi. Further gain enhancement across the entire operating bandwidth without increasing the antenna size is achieved in the subsequent stage through the integration of AZIM unit cells.

AZIM unit cell design and analysis

Metamaterials whose refractive index approaches zero, defined as $\eta = \sqrt{\varepsilon_{\text{eff}}\mu_{\text{eff}}}$, are referred to as ZIMs. These artificial structures exhibit unique EM properties that enable precise manipulation of wave propagation, including phase uniformity and field collimation. In the proposed antenna design, AZIM unit cells are employed to collect the radiated EM energy and collimate it into a narrow beam directed along the antenna broadside. Such materials, characterized by conditions where $\varepsilon = \mu = 0$, or $\varepsilon = 0$ with $\mu \neq 0$, or $\mu = 0$ with $\varepsilon \neq 0$, are capable of suppressing backscattered reflections while simultaneously enhancing forward radiation, thereby improving antenna directivity and realized gain [44].

For periodic metallic patterns printed on a dielectric substrate, the effective permittivity ε_{eff} approaches zero as the excitation frequency approaches the plasma frequency ω_p. This frequency-dependent behavior is expressed via Equation 18

$$\varepsilon_{\text{eff}} = 1 - \frac{\omega_p^2}{\omega^2}, \tag{18}$$

where ω is the angular frequency of the incident EM wave. To shift the plasma frequency into the microwave regime, the geometry of the unit cells must be carefully tailored. Pendry et al. [45] demonstrated that increasing the effective inductance and capacitance of the unit cell structure lowers ω_p, thereby enabling plasmonic behavior at microwave frequencies. The effective EM parameters of the AZIM unit cell are retrieved using the scattering-parameter-based method proposed by Smith et al. [46, 47]. When a normally incident plane wave excites the unit cell, the reflection (S_{11}) and transmission (S_{21}) coefficients are obtained from full-wave simulations. Using these parameters, the effective wave impedance Z and refractive index η are calculated using Equations 19 and 20.

$$Z = \pm\sqrt{\frac{(1+S_{11})^2 - S_{21}^2}{(1-S_{11})^2 - S_{21}^2}}, \tag{19}$$

https://doi.org/10.1017/S1759078726103353 Published online by Cambridge University Press

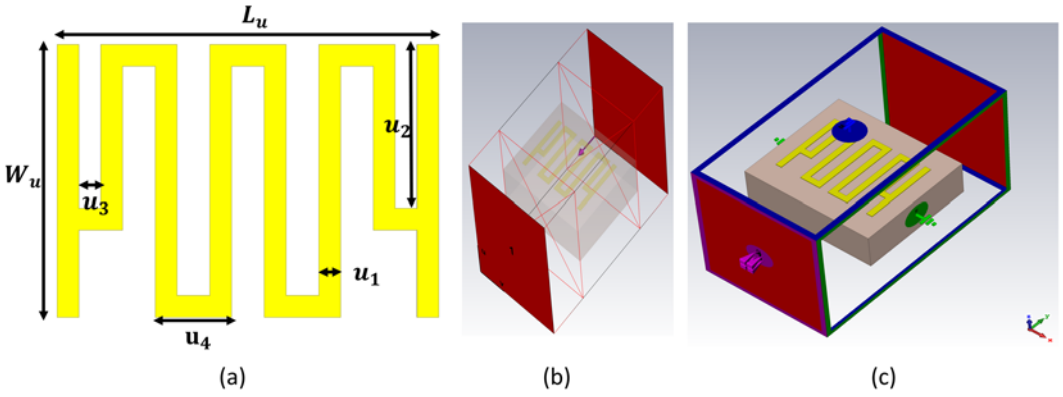


Figure 9. AZIM metamaterial unit cell: (a) optimized geometrical parameters ($L_u = 4.6$ mm, $W_u = 5$ mm, $u_1 = 0.2$ mm, $u_2 = 3.5$ mm, $u_3 = 0.5$ mm, $u_4 = 0.7$ mm); (b) simulation setup with ports de-embedded to the unit cell edges for accurate S-parameter extraction; and (c) applied boundary conditions with wave propagation and field orientations for unit cell analysis.

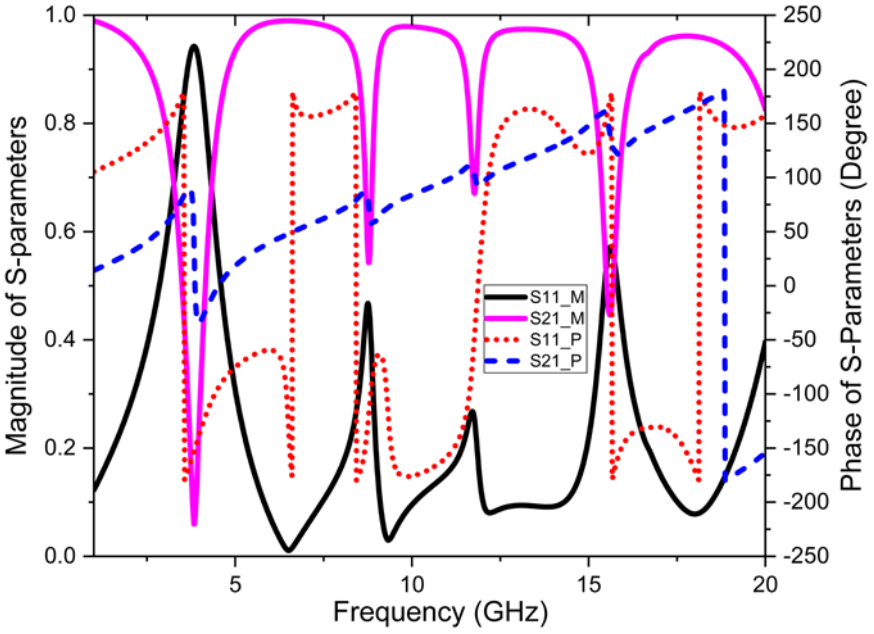


Figure 10. Magnitude and phase response of the simulated S-parameters (S_{11} and S_{21}) for the proposed AZIM unit cell. The left vertical axis indicates the magnitude of the scattering parameters, while the right vertical axis represents the phase in degrees.

$$\eta = \frac{1}{k_0 d}\left\{\mathrm{Im}\left[\ln\left(e^{jnk_0 d}\right)\right] + 2p\pi - j\,\mathrm{Re}\left[\ln\left(e^{jnk_0 d}\right)\right]\right\}, \tag{20}$$

where k_0 is the free-space wave number, d is the unit-cell thickness, where p is an integer chosen to maintain the physical branch of the refractive index. The integer p is computed using Equation 21.

$$p = \mathrm{round}\left\{-\frac{1}{2\pi}\left[\ln\left(\frac{S_{21}}{1 - S_{11}\left(\frac{Z-1}{Z+1}\right)}\right)\right]\right\} \tag{21}$$

The configuration and simulation setup of the AZIM unit cell using CST-MWS are illustrated in Figure 9. Figure 9(a) shows the proposed meander-line-based AZIM unit cell geometry employed to achieve near-zero refractive index characteristics. To accurately extract the scattering parameters, a de-embedded port arrangement is adopted, as depicted in Figure 9(b). Figure 9(c) presents the applied boundary conditions, where the electric field is orientated along the x-direction, the magnetic field along the z-direction, and the EM wave propagates in the y-direction. The optimized unit cell is fabricated on the same FR-4 substrate with a thickness of 0.8 mm to maintain compatibility with the proposed antenna.

The simulated de-embedded magnitude and phase of reflection and transmission coefficients of the proposed AZIM unit cell are analyzed in Figure 10. The magnitude response, shown in Figure 10, demonstrates a high transmission coefficient ($|S_{21}|$) alongside a suppressed return loss ($|S_{11}|$), signifying efficient energy tunneling and minimal reflection at the design frequency. Furthermore, the phase of the transmission coefficient (S_{21}) is illustrated in Figure 10 (scale shown in right side of the figure). The observed linear phase response within the operational band confirms the near-zero refractive index characteristic of the medium. This linear phase variation S_{21} indicates that the EM wave propagates through the anisotropic slab with an infinite phase velocity, maintaining spatial phase uniformity – a hallmark of ZIM structures [46]. After de-embedding the S-parameters to the unit-cell boundaries, a MATLAB-based retrieval algorithm is employed to extract the effective parameters. As shown in Figure 11, the AZIM cell exhibits near-zero permittivity in the frequency range of 5–19.5 GHz, confirming its suitability for enhancing antenna gain and directivity in the higher operating band.

https://doi.org/10.1017/S1759078726103353 Published online by Cambridge University Press

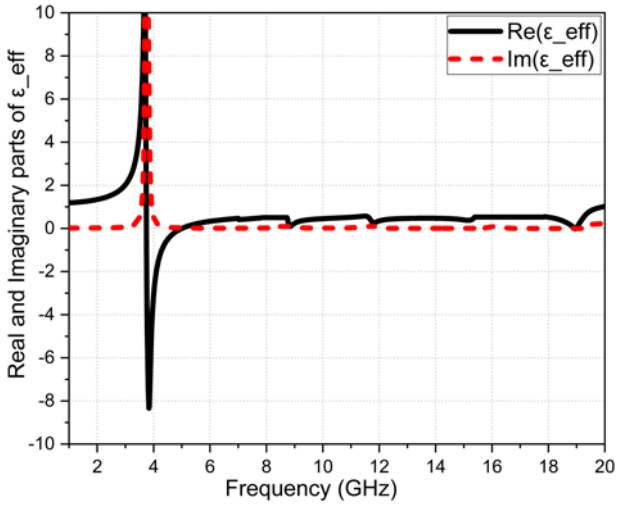


Figure 11. Retrieved effective permittivity (ϵ_{eff}) of the proposed AZIM unit cell showing real and imaginary components versus frequency.

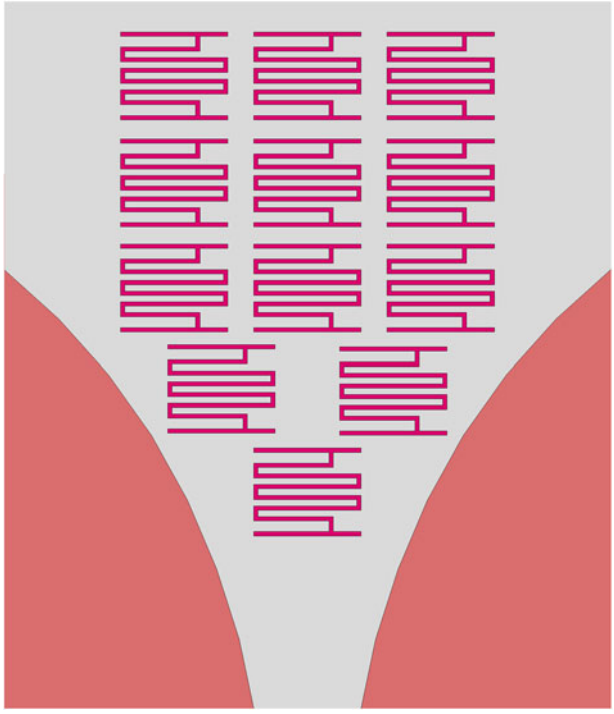


Figure 12. Enlarged view illustrating the placement of AZIM metamaterial unit cells loaded within the tapered slot region of the proposed antenna, highlighting their integration along the taper profile.

AZIM cell loaded on Stage 6 antenna: design and analysis

The integration of AZIM cells into the proposed antenna requires careful consideration of the antenna geometry, excitation mechanism, and beam orientation. The placement of the AZIM cells must ensure that the feed structure and impedance matching characteristics of the antenna remain unaffected. Moreover, the number of AZIM cells is governed by the symmetry of the tapered slot profile and the available spacing between the radiating arms. To identify the optimal configuration, extensive full-wave simulations were performed using CST-MWS, with the primary objective of maximizing forward radiation while preserving UWB impedance matching. Through an iterative optimization process, the most effective location for embedding the AZIM cells was identified within the tapered slot region, as illustrated in Figure 1(a), with a magnified view shown in Figure 12. This placement enables strong interaction between the radiated EM fields and the AZIM cells, facilitating efficient field collimation without introducing additional mismatch.

The optimized antenna configuration incorporating AZIM unit cell loading in stage 6 is referred to as the proposed antenna. To further elucidate the underlying physical mechanism, the electric-field distributions of Stage 1 (reference antenna) and the proposed antenna are examined at 10 GHz, as shown in Figure 13. Compared to the reference antenna, the AZIM-loaded configuration exhibits noticeably flatter phase fronts compared to spherical fronts in the reference antenna and concentrated field regions in the forward direction, indicating a strong focusing effect. A 3-D radiation pattern at 10 GHz of the reference and the proposed antenna are shown in Figure 14(a) and (b) respectively. The three-dimensional radiation patterns at 10 GHz indicate that the AZIM-cell-loaded DTSVA exhibits improved beam shaping with enhanced forward gain and effective sidelobe suppression compared to the reference antenna. These results confirm that embedding AZIM cells within the tapered slot structure is an effective approach for improving antenna gain and directivity without compromising the wide impedance range bandwidth.

Results and discussion

The performance of the proposed antenna and the reference antenna was initially investigated through full-wave EM simulations using CST-MWS (v2016) and subsequently validated through experimental measurements. The measurements were performed using a Rohde & Schwarz ZVA50 Vector Network Analyzer (VNA) (10 MHz–50 GHz), which fully covers the 1–20 GHz band, eliminating the need for segmented measurements. A full short-open-load-through (SOLT) calibration was conducted prior to testing to ensure accuracy. S-parameters, gain, and radiation patterns were measured in an anechoic chamber using a standard two-antenna setup with broadband horn antennas. High-quality RF cables and SMA connectors were employed to minimize mismatch and measurement uncertainties. The fabricated prototypes of the reference antenna and the proposed antenna are shown in Figure 15. A comprehensive evaluation was carried out in both the frequency and time domains. In the frequency domain, antenna performance was assessed in terms of VSWR, radiation efficiency, far-field radiation patterns, and peak realized gain. Time-domain analysis focused on the group delay and the transmission transfer function, represented by the magnitude of S_{21} (isolation), to verify the suitability of the antenna for UWB and imaging applications. The simulated and measured VSWR and S_{11} responses of both antennas are presented in Figure 16 and 17, respectively. A good agreement between simulation and measurement is observed across the operating band for both the reference and proposed antennas. The proposed antenna exhibits distinct band-rejection characteristics, evidenced by sharp VSWR peaks or $S_{11} > -2.5$ dB at the notched frequencies, while maintaining VSWR < 2 or approximately $S_{11} < -10$ dB over the remaining UWB range. Good agreement between the simulated and measured results is observed, validating the design approach. Minor discrepancies between the simulated and measured results are mainly attributed to fabrication tolerances and measurement uncertainties. The variation in radiation efficiency of the reference

https://doi.org/10.1017/S1759078726103353 Published online by Cambridge University Press

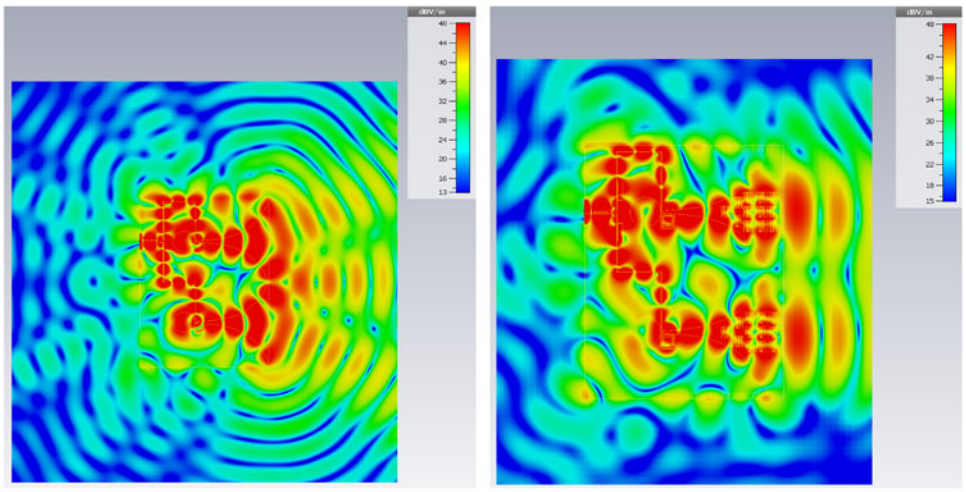


Figure 13. Electric field distribution at 10 GHz: (a) reference DTSVA antenna and (b) proposed AZIM unit-cell-loaded DTSVA antenna.

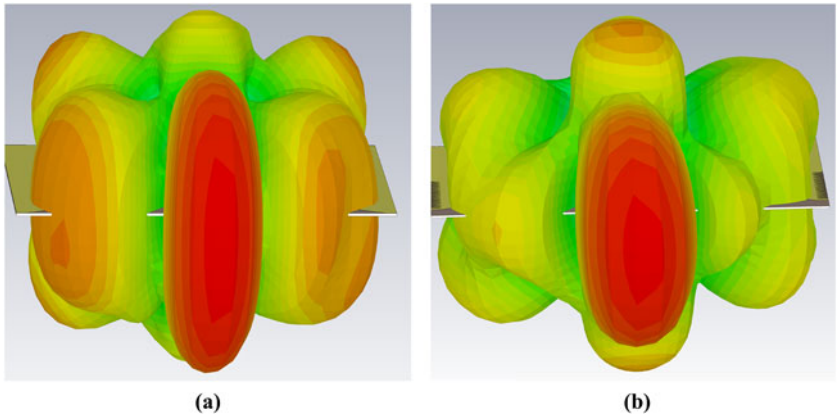


Figure 14. Three-dimensional radiation patterns at 10 GHz for (a) the reference DTSVA antenna and (b) the proposed AZIM-loaded DTSVA antenna.

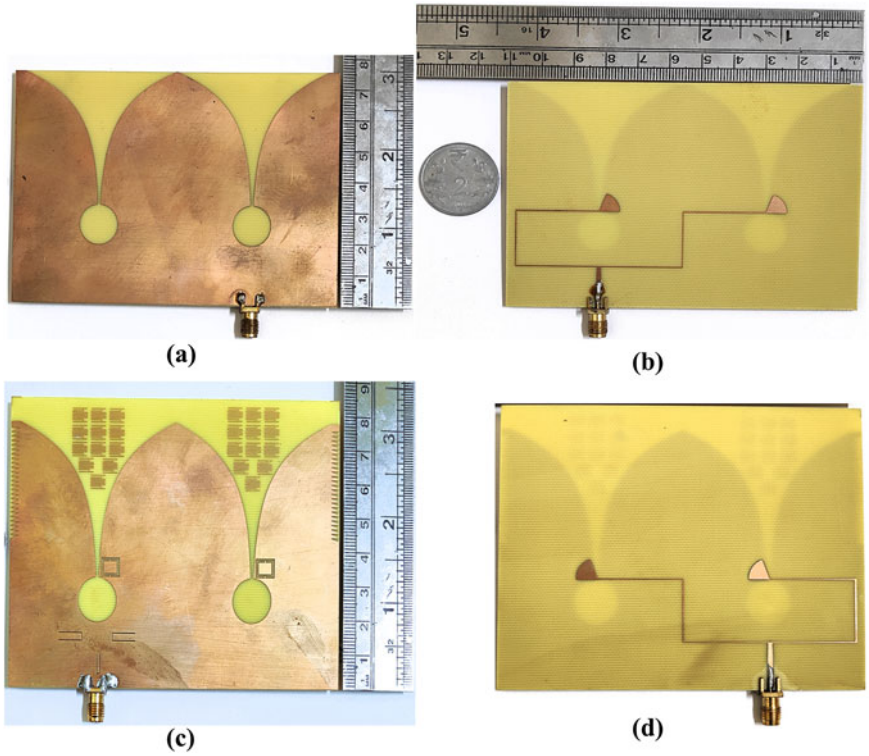


Figure 15. Fabricated prototypes of the antennas: (a) top layer and (b) bottom layer of the reference DTSVA antenna; and (c) top layer and (d) bottom layer of the proposed AZIM-loaded DTSVA antenna.

https://doi.org/10.1017/S1759078726103353 Published online by Cambridge University Press

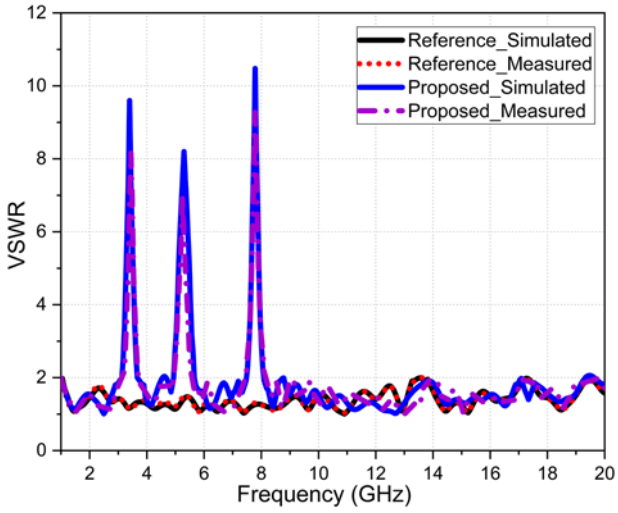


Figure 16. Simulated and measured VSWR responses of the reference and proposed AZIM-loaded DTSVA antennas.

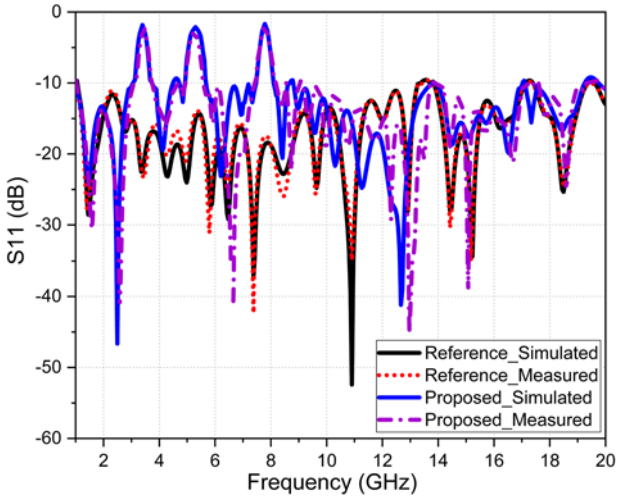


Figure 17. Simulated and measured return loss responses of the reference and proposed AZIM-loaded DTSVA antennas.

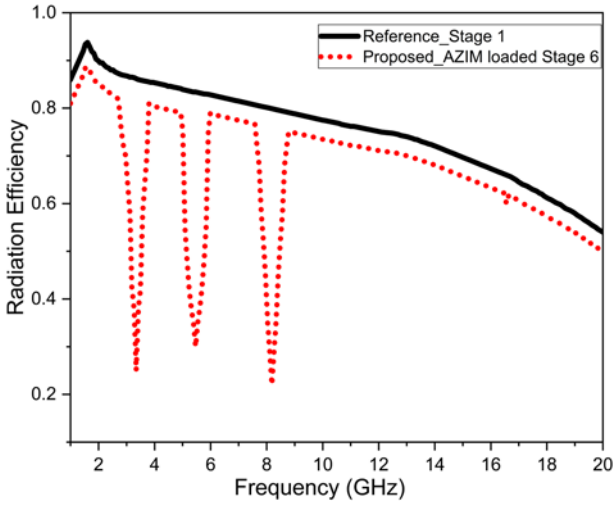


Figure 18. Simulated radiation efficiency comparison of the reference DTSVA and proposed AZIM-loaded DTSVA antennas.

DTSVA and the proposed AZIM unit-cell- and resonator-loaded DTSVA is illustrated in Figure 18. Due to the lossy nature of the FR-4 substrate, a gradual reduction in radiation efficiency from approximately 92% to 55% is observed with increasing frequency for both designs. Despite this degradation, the proposed antenna maintains radiation efficiency above 55% up to 19.6 GHz, confirming its effective operation over the wide frequency range of 2.8–19.5 GHz. The sharp efficiency dips at the rejected bands further validate the intended band-notch behavior introduced by the AZIM loading.

The measurement setup of the proposed antenna within an anechoic chamber is illustrated in Figure 19(a) to evaluate the far-field radiation patterns and gain characteristics. An enlarged perspective of the fabricated antenna prototype mounted on the positioner is shown in Figure 19(b), while the experimental configuration for measuring the return loss and impedance bandwidth using a calibrated VNA is presented in Figure 19(c).

The two-dimensional (2-D) polar far-field radiation characteristics of the reference and proposed antennas were analyzed at 4, 7, 11, 15, and 18 GHz using simulated and measured E-plane (XY-plane, $\theta = 90^{\circ}$) and H-plane (XZ-plane, $\phi = 0^{\circ}$) radiation patterns, as shown in Figure 20(a)–(e) and 21(a)–(e), respectively. The 2-D polar radiation patterns in both planes demonstrate that the proposed AZIM-loaded DTSVA maintains stable end-fire radiation characteristics across the 4–18 GHz band. While the radiation patterns at 4 GHz remain nearly identical to those of the reference antenna due to the AZIM unit cell's operational threshold of 5 GHz (as shown in Figure 11), a noticeable narrowing of the main lobe is observed from 7 to 18 GHz. This beam sharpening confirms that the AZIM loading effectively compensates for phase errors at the antenna aperture, transforming spherical wavefronts into planar ones and thereby enhancing directivity. The close agreement between simulated and measured results further validates the effectiveness of the aperiodic metamaterial integration for high-gain wideband applications.

A comparison between the simulated and measured peak realized gains of the proposed antenna and the measured peak realized gain of the reference antenna is presented in Figure 22. The incorporation of AZIM unit cells in Stage 6 results in a significant gain enhancement over the frequency range of 5–19 GHz.

A maximum gain improvement of approximately 3.8 dBi is observed at 7.2 GHz, yielding a peak realized gain of 12.45 dBi. Furthermore, compared with a single-slot TSVA of identical physical dimensions, the AZIM-loaded double-tapered slot antenna exhibits an additional peak realized gain improvement of approximately 4.7 dBi. Deep gain nulls at the notched bands further confirm effective selective interference suppression while maintaining high gain across the remaining operating band.

The close agreement between simulated and measured results (as shown in Figures 16, 17, 20, 21, and 22) is attributed to the inherently smooth impedance transition of the Vivaldi antenna, which reduces sensitivity to fabrication tolerances. Additionally, accurate simulation settings, proper SOLT calibration, and measurements performed in an anechoic environment contribute to minimizing discrepancies. The use of a high-quality SMA connector further ensures reliable wideband performance. Minor discrepancies, though not visually prominent, arise from controlled measurement uncertainties such as FR-4 dielectric constant

https://doi.org/10.1017/S1759078726103353 Published online by Cambridge University Press

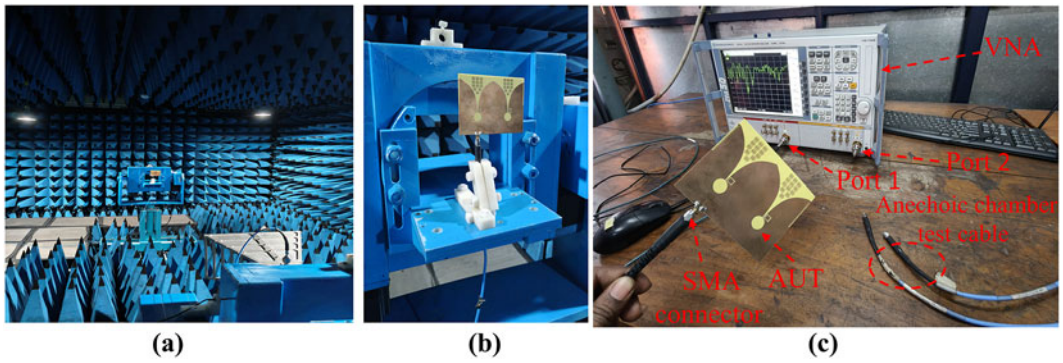


Figure 19. (a) Anechoic chamber, (b) zoom view, and (c) measured S_{11} through VNA of the proposed antenna in open space.

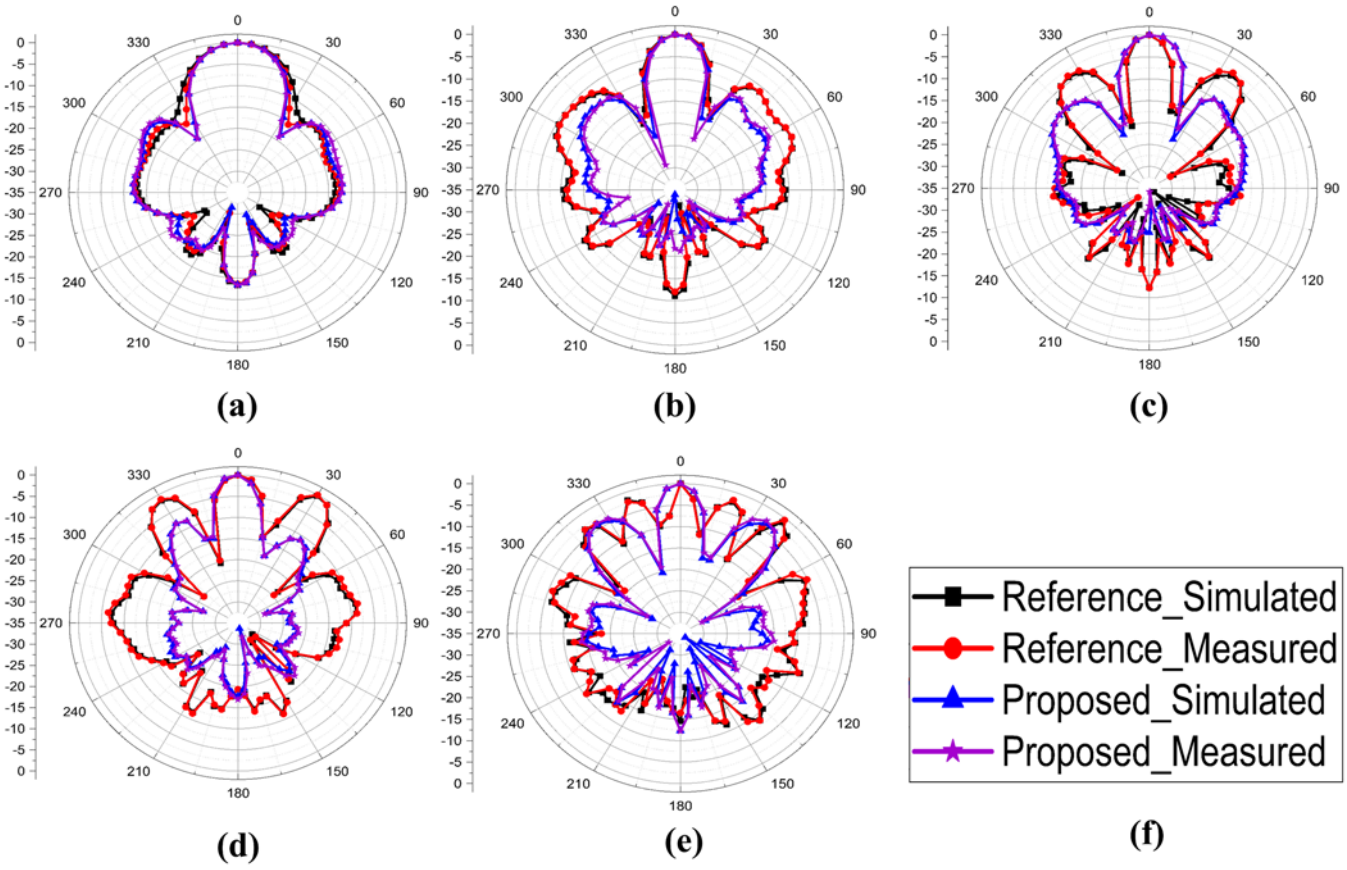


Figure 20. Two-dimensional polar radiation patterns in the E-plane showing simulated and measured results of the reference and proposed AZIM-loaded DTSVA antennas at (a) 4 GHz, (b) 7 GHz, (c) 11 GHz, (d) 15 GHz, and (e) 18 GHz; and (f) legend used for comparison.

variation ($\pm$0.2–0.4), SMA connector and soldering parasitics, and cable losses with VNA repeatability.

The measured group delay and isolation responses of the reference and proposed antennas are shown in Figure 23. The obtained measurements were performed using a face-to-face far-field configuration. The group delay (right vertical axis) is measured in the far-field region with an inter-antenna separation $d > 2.4$ m at the lowest frequency of 1 GHz, while the isolation (S_{21}, left vertical axis) is measured with a fixed separation of $d = 500$ mm. The group delay remains nearly constant over the 1–20 GHz range, indicating good time-domain fidelity. Pronounced peaks are observed at 3.5, 5.6, and 8.2 GHz, confirming effective signal rejection at the designed notched bands. The S_{21} characteristics, simulated using two identical antennas separated by 500 mm, exhibit deep transmission nulls at the same frequencies for the proposed antenna, whereas the reference antenna shows smooth transmission across the entire band. Outside the notched regions, comparable S_{21} levels indicate stable UWB transmission behavior. The gradual reduction in S_{21} magnitude at higher frequencies is primarily attributed to increased dielectric and conductor losses of the FR-4 substrate, which become more pronounced at higher frequencies and lead to increased transmission attenuation.

The group delay was measured using a Rohde & Schwarz ZVA50 VNA in a two-antenna transmission configuration. Two identical

https://doi.org/10.1017/S1759078726103353 Published online by Cambridge University Press

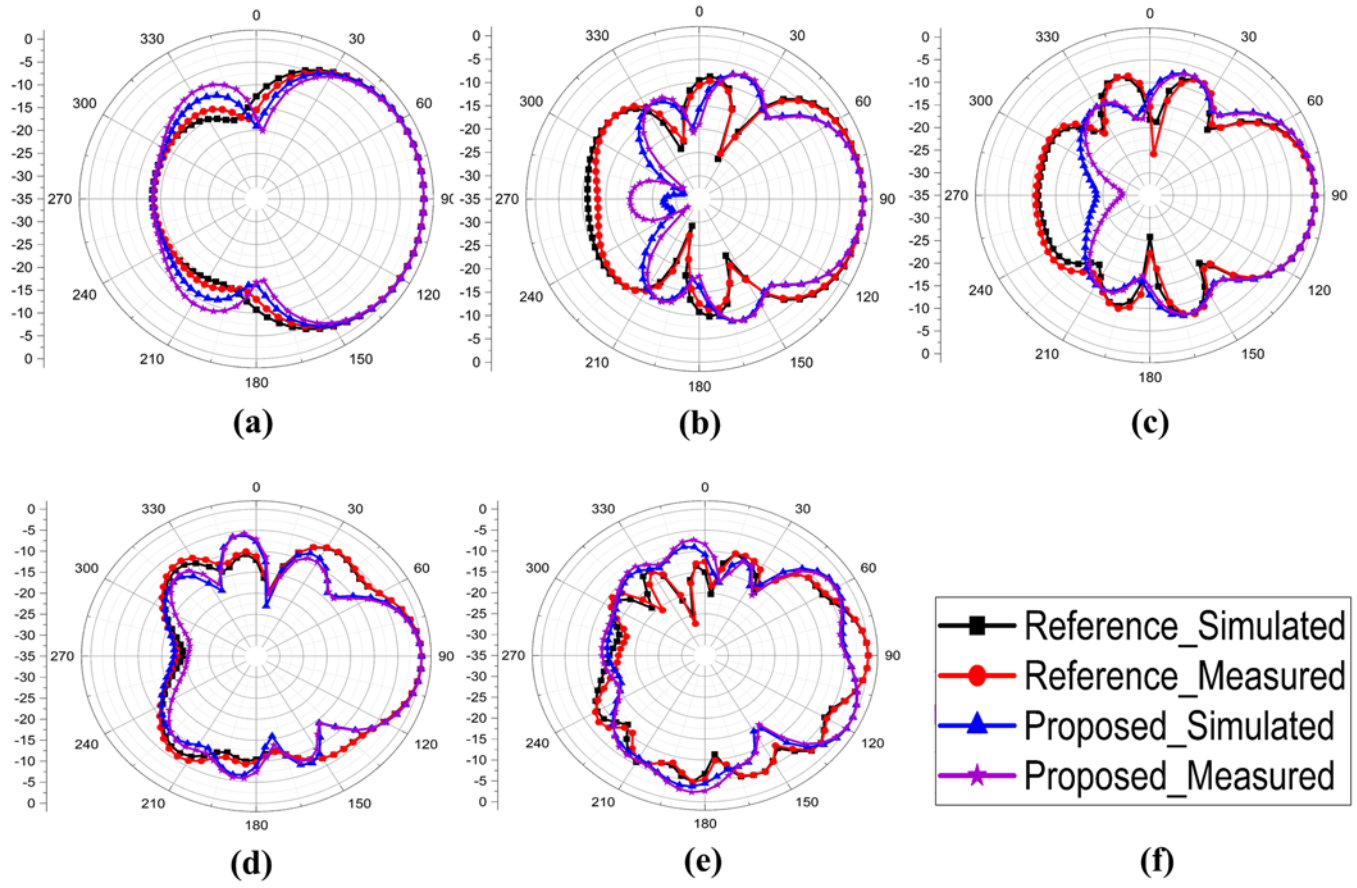


Figure 21. Two-dimensional polar radiation patterns in the H-plane showing simulated and measured results of the reference and proposed AZIM-loaded DTSVA antennas at (a) 4 GHz, (b) 7 GHz, (c) 11 GHz, (d) 15 GHz, and (e) 18 GHz; and (f) legend used for comparison.

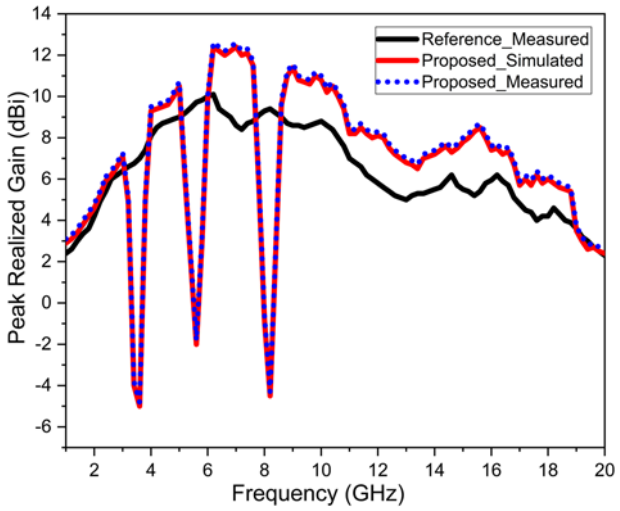


Figure 22. Peak realized gain versus frequency showing simulated and measured results of the proposed AZIM-loaded DTSVA antenna and measured results of the reference DTSVA antenna.

antennas were placed in a face-to-face arrangement under far-field conditions ($R > \frac{2D^2}{\lambda}$), where λ corresponds to the wavelength at the highest operating frequency (20 GHz), and connected to Port 1 and Port 2 using low-loss coaxial cables. A full two-port calibration Through-Open-Short-Match (TOSM) was performed to eliminate cable and connector effects. The frequency range was set from 1 to 20 GHz with 1000 sweep points and a reduced IF bandwidth (5 KHz) to improve phase accuracy. The group delay was obtained from the negative derivative of the transmission phase with respect to angular frequency. Since a two-antenna setup was used, the group delay of a single antenna is approximated as half of the measured value.

A comparison of the proposed antenna with recently reported works is presented in Table 2. Based on this comparative study, it is observed that most reported TSVA/AVA designs achieve a wide impedance bandwidth at the expense of larger antenna dimensions, expensive low-loss substrates, or limited notch functionality. Several reported works employ single-band or dual-band notch techniques using CSRRs, slots, or resonant strips, while gain enhancement is commonly achieved through corrugation, metamaterial loading, or director elements. Many of these designs either lack multiple notch bands or rely on complex geometries and high-performance substrates. In contrast, the proposed double-slot DTSVA achieves an ultra-wide impedance bandwidth of 1–20 GHz using a low-cost FR-4 substrate while incorporating three well-defined notch bands to suppress WiMAX, WLAN, and X-band interferences. Moreover, the combined integration of AZIM cell loading and corrugation results in a noticeable gain enhancement of up to 3.8 dBi, making the proposed antenna a compact,

https://doi.org/10.1017/S1759078726103353 Published online by Cambridge University Press

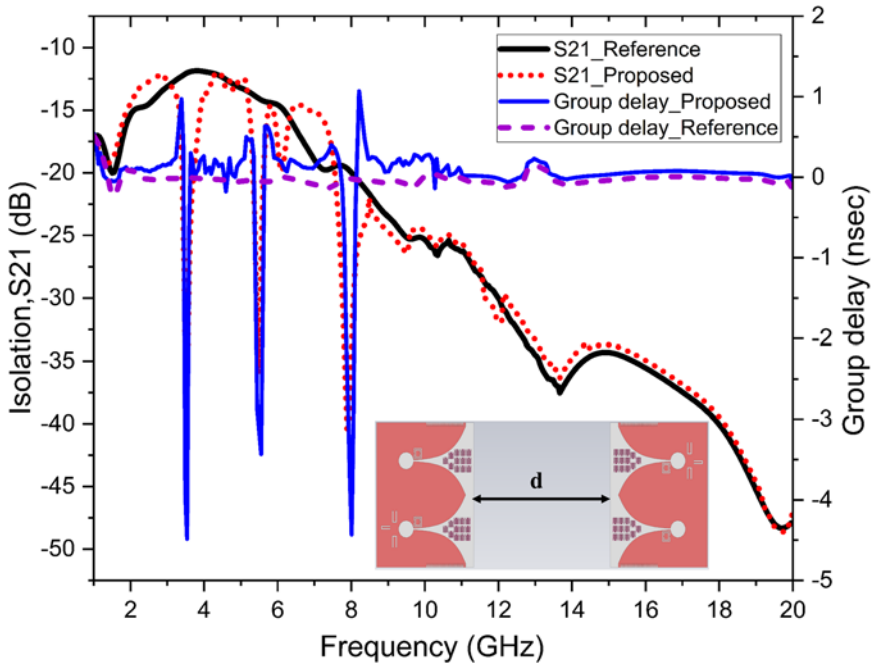


Figure 23. Measured group delay and isolation (S_{21}) responses of the reference and proposed antennas.

Table 2. Comparative performance analysis of the proposed DTSVA antenna with recently reported designs

Ref.	Normalized size (λ_0^3), Physical size (W × L × H) mm^3	Substrate	BW (GHz)	Type	Notch bands (GHz)	Gain enhancement
[18]	$(1.15 \times 0.38 \times 0.012)\lambda_0^3$ (150 × 50 × 1.6)	FR-4	2.3–30	TSVA	3.3–8.2 (CSRR)	Corrugated; 5.8 dBi
[19]	$(0.25 \times 0.08 \times 0.003)\lambda_0^3$ (60 × 20 × 0.78)	RF-35	1.25–12	AVA	5.0 (T-slot)	Cut-out; 3 dBi
[20]	$(0.69 \times 0.67 \times 0.003)\lambda_0^3$ (104 × 100 × 0.5)	RO4003	2–9	AVA	3.3–3.6	None
[21]	$(0.63 \times 0.39 \times 0.007)\lambda_0^3$ (73 × 45 × 0.78)	R5880	2.6–13.7	TSVA	4.5–6.6	None
[34]	$(0.52 \times 0.52 \times 0.008)\lambda_0^3$ (50 × 50 × 0.8)	FR-4	3.1–10.6	TSVA	4.4–5.1	AZIM; 2.6 dBi
[48]	$(0.69 \times 0.33 \times 0.002)\lambda_0^3$ (260 × 121.9 × 0.76)	IS680	0.8–30.5	AVA	None	Slots + Dir.; 3.1 dBi
[49]	$(1.92 \times 0.41 \times 0.004)\lambda_0^3$ (282 × 60 × 0.508)	R5880	2.0–23.1	TSVA	None	None
[50]	$(2.64 \times 1.30 \times 0.022)\lambda_0^3$ (61 × 30 × 0.508)	R5880	13–20	AVA	None	Meta; 3.1 dBi
[51]	$(1.20 \times 0.70 \times 0.007)\lambda_0^3$ (180 × 105.5 × 1)	F4B	2–13.4	D-TSVA	None	Meta; 3.1 dBi
[52]	$(2.27 \times 0.68 \times 0.057)\lambda_0^3$ (20 × 6 × 0.5)	R5880	34–43.8	AVA	None	SSRR; 4.6 dBi
Proposed	$(0.366 \times 0.28 \times 0.003)\lambda_0^3$ **(110 × 84 × 0.8)**	**FR-4**	**1–20**	**D-TSVA**	**3.3–3.8, 5.15–5.85, 7.9–8.4**	**AZIM; 3.8 dBi**

Note: Normalized dimensions are calculated with respect to the free-space wavelength (λ_0) at the lowest operating frequency.

cost-effective, and high-performance solution compared with existing designs reported in the literature.

Future work

Future work may explore the development of array-based implementations of the proposed antenna to achieve higher directivity and improved spatial resolution for imaging applications. The incorporation of tunable or reconfigurable resonators can provide adaptive band-notch characteristics, making the antenna suitable for dynamic and multi-standard wireless environments.

Conclusion

A compact corrugated DTSVA has been designed, optimized, and experimentally validated for UWB applications. The proposed antenna operates over an ultra-wide frequency range of 1–20 GHz and incorporates triple band-notch characteristics to suppress interference from WiMAX, WLAN, and X-band uplink systems. The obtained notched bands are realized through the integration of a CSRR and U-shaped slots. Owing to the presence of the CSRR and U-slots, a slight degradation in peak realized gain is observed in the 1–3 GHz frequency range. To compensate for this effect, triangular slit corrugation techniques are employed, resulting in improved gain performance. To further enhance the radiation characteristics, an AZIM unit cell is embedded within

https://doi.org/10.1017/S1759078726103353 Published online by Cambridge University Press

the tapered slot region. This integration significantly enhances forward radiation and provides a gain improvement of up to 3.8 dBi over the 5–19 GHz band without increasing the overall antenna size. The antenna geometry is systematically optimized through extensive parametric studies to achieve a wide impedance bandwidth, stable radiation characteristics, and effective notch performance. Comprehensive numerical simulations and experimental measurements confirm the robust performance of the proposed antenna in terms of VSWR, peak realized gain, radiation efficiency, group delay, and far-field radiation patterns. A close agreement between simulated and measured results validates the accuracy of the proposed design. Owing to its compact size, low-cost FR-4 substrate, selective interference suppression, and enhanced gain performance, the proposed antenna is well-suited for microwave imaging, radar sensing, material characterization, and portable UWB communication systems. Future work may extend the proposed concept to antenna arrays and advanced metamaterial configurations for further performance enhancement.

Acknowledgements. The authors acknowledge the Department of Electronics and Communication Engineering, IIT (ISM) Dhanbad, for providing access to the DST-FIST laboratory facilities (project reference: SR/FST/ET-I/2019/289). Special thanks are extended to Dr. Ravi Kumar Gangwar, in charge of the DST-FIST lab, for his support in successfully carrying out the scheduled measurements using the anechoic chamber and VNA facilities.

Competing interests. The author(s) declare none.

References

1. **Wang M, Crocco L, Li M and Cavagnaro M** (2024) Slot-loaded Vivaldi antenna for biomedical microwave imaging applications: Influence of design parameters on antenna dimensions and performances. *Sensors* **24**(16), 5368.
2. **Amador M, Rouco A, Albuquerque D and Pinho P** (2024) Ultra-wideband Vivaldi antenna for through-wall-radar applications. In *IEEE-APS Topical Conference on Antennas and Propagation in Wireless Communications (APWC)*, pp. 154–158. Lisbon, Portugal.
3. **Saleh S, Timmons N, Morrison J and Ismail W** (2024) Compact linearly polarized 5G Vivaldi non-uniform slot filtering antenna. *Ain Shams Engineering Journal* **15**(2), 102364.
4. **Joy SCPV and Singh H** (2023) A novel design of low RCS Vivaldi antenna for electronic warfare application. *In Proceedings of the 4th International Conference on Communications, Computing and Industry 6.0 (C216)*, pp. 1–7.
5. **Ramyasree G and Suman N** (2023) Dual-band 4-port Vivaldi MIMO antenna for 5G mmWave applications at 28/39 GHz. *Progress in Electromagnetics Research M* **119**, 13–24.
6. **Gibson PJ** (1979) The Vivaldi aerial. *European Microwave Conference (EuMC), 9th edition*, pp. 101–105. Brighton, UK.
7. **Gazit E** (1988) Improved design of the Vivaldi antenna. *IEEE Proceedings H: Microwaves, Antennas and Propagation* **135**(2), 89–92.
8. **Kim SG and Chang K** (2004) A low cross-polarized antipodal Vivaldi antenna array for wideband operation. *IEEE Antennas and Propagation Society International Symposium (APS Symposium)* **3**, 2269–2272.
9. **Vu TA, Dooghabadi MZ, Sudalaiyandi S, Hjortland HA, Næss Ø, Lande TS, Hamran SE** (2009) UWB Vivaldi antenna for impulse radio beamforming. *NORCHIP Conference (Proceedings)*, pp. 1–5. Trondheim, Norway.
10. **Akhtar J** (2008) *Microwave Imaging: Reconstruction of One-Dimensional Permittivity Profiles*. Germany: VDM Verlag.
11. **Akhtar MJ, Feher LE and Thumm M** (2006) A waveguide-based two-step approach for measuring complex permittivity tensor of uniaxial composite materials. *IEEE Transactions on Microwave Theory and Techniques* **54**(5), 2011–2022.
12. **Hasar UC** (2009) Water-to-cement ratio prediction using ANNs from non-destructive microwave measurements. *Progress in Electromagnetics Research (PIER)* **94**, 311–325.
13. **Saleh S, Saeidi T and Timmons N** (2024) Simple compact UWB Vivaldi antenna arrays for breast cancer detection. *Telecommunication* **5**(2), 312–332.
14. **Zhao L** (2024) Compact circular-shaped MIMO antenna covering UWB bandwidth with band-notched characteristics. *IEEE Access* **12**, 32762–32771.
15. **Parthiban N and Ismail MM** (2022) Quad-band notch UWB antenna using SLR circuits. *Progress in Electromagnetics Research C* **124**, 11–22.
16. **Zhang Y** (2008) Planar UWB antennas with multiple notched bands. *IEEE Transactions on Antennas and Propagation* **56**(9), 3063–3068.
17. **Sarkar D, Srivastava KV and Saurav K** (2014) Compact triple band-notched UWB monopole antenna. *IEEE Antennas and Wireless Propagation Letters* **13** 396–399.
18. **Nurhayati N, Zulkifli FY, Setijadi E, Sukoco BE, Yasin MNM and De Oliveira AM** (2024) Bandwidth and gain improvement with notched-band characteristics of a SWB wave coplanar Vivaldi antenna using CSRR. *IEEE Access* **12**, 16926–16938.
19. **Lixia D, Qi H, Huang T and Wu T** (2022) Compact antipodal Vivaldi antenna with gain enhancement and notched-band characteristics based on D-CRLH metamaterial. *Materials Research Express* **9**(2), 025803.
20. **Yang Z, Huang J and Yang N** (2017) An antipodal Vivaldi antenna with band-notched characteristics for ultra-wideband applications. *AEU – International Journal of Electronics and Communications* **76**, 152–157.
21. **Xiong M, Duan J and Zhang B** (2020) A band-rejection Vivaldi antenna with high selectivity using hybrid HRW/CCLL. *International Journal of Antennas and Propagation 2020*, (1), 2061948.
22. **Xu Y, Wang J, Ge L, Wang X and Wu W** (2017) Design of a notched-band Vivaldi antenna with high selectivity. *IEEE Antennas and Wireless Propagation Letters* **17**(1), 62–65.
23. **Chaabane A and Guerroui M** (2023) A planar dual notched-band Vivaldi antenna for wireless communication applications. *Defence Science Journal* **74**, 79–84.
24. **Yang D, Liu S, Chen M and Wen Y** (2015) A compact Vivaldi antenna with triple band-notched characteristics. *IEEE 6th International Symposium on Microwave, Antenna, Propagation, and EMC Technologies (MAPE)*, 216–219. Shanghai, China.
25. **Liu X** (2013) The band-notch sensitivity of Vivaldi antenna toward CSRRs. *Progress in Electromagnetics Research Letters* **43**, 125–135.
26. **Yang D** (2016) A Vivaldi antenna with switchable and tunable band-notch characteristics. *Progress in Electromagnetics Research C* **68**, 75–83.
27. **Paul LC and Islam MM** (2021) A super-wideband directional compact Vivaldi antenna for lower 5G and satellite applications. *International Journal of Antennas and Propagation*, 2021, (1), 8933103.
28. **Wang YW** (2015) Conformal corrugated edges for Vivaldi antenna to obtain improved low-frequency characteristics. *Progress in Electromagnetics Research C* **60**, 75–81.
29. **Moosazadeh M and Kharkovsky S** (2015) Design of ultra-wideband antipodal Vivaldi antenna for microwave imaging applications. In *IEEE International Conference on Ultra-Wideband (ICUWB)*, pp. 1–4. Montereal, Canada. https://doi.org/10.1109/ICUWB.2015.7324435.
30. **Nassar TI and Weller TM** (2015) A novel method for improving antipodal Vivaldi antenna performance. *IEEE Transactions on Antennas and Propagation* **63**(7), 3321–3324.
31. **Islam TM, Mahmud MZ, Kibria S and Samsuzzaman M** (2019) A low-cost and portable microwave imaging system for breast tumor detection using UWB directional antenna array. *Scientific Reports* **9**(1), 1–13..
32. **Cicchetti R, Cicchetti V, Faraone A, Foged L and Testa O** (2021) A compact high-gain wideband lens Vivaldi antenna for wireless communications and through-the-wall imaging. *IEEE Transactions on Antennas and Propagation* **69**(6), 3177–3192.
33. **Cicchetti R, Cicchetti V, Faraone A and Testa O** (2021) A class of lightweight spherical-axicon dielectric lenses for high-gain wideband antennas. *IEEE Access* **9**, 151873–151887.

https://doi.org/10.1017/S1759078726103353 Published online by Cambridge University Press

34. **Bhaskar M, Johari E, Akhter Z and Akhtar MJ** (2016) Gain enhancement of the Vivaldi antenna with band-notch characteristics using zero-index metamaterial. *Microwave and Optical Technology Letters* **58**(1), 233–238.
35. **Usha P and Krishnan C** (2020) Epsilon-near-zero metasurface for ultra-wideband antenna gain enhancement and radar cross-section reduction. *AEU-International Journal of Electronics and Communications* **119**, 153167.
36. **Sun M, Chen ZN and Qing X** (2013) Gain enhancement of 60-GHz antipodal tapered slot antenna using zero-index metamaterial. *IEEE Transactions on Antennas and Propagation* **61**(4), 1741–1746.
37. **Das S and Mitra D** (2018) A compact wideband flexible implantable slot antenna design with enhanced gain. *IEEE Transactions on Antennas and Propagation* **66**(8), 4309–4314.
38. **Portosi V** (2023) A novel L-shaped metalens for ultra-wideband antenna gain improvement. *Applied Sciences* **13**(8), 4802.
39. **Shi X** (2021) A high-gain antipodal Vivaldi antenna with director and metamaterial at 1-28 GHz. *IEEE Antennas and Wireless Propagation Letters* **20**(12), 2432–2436.
40. **Jaiswal PK, Bhattacharya R and Kumar A** (2023) A UWB antipodal Vivaldi antenna with high gain using metasurface and notches. *AEU-International Journal of Electronics and Communications* **159**, 154473.
41. **Marqués R** (2003) Comparative analysis of edge- and broadside-coupled split-ring resonators for metamaterial design: Theory and experiments. *IEEE Transactions on Antennas and Propagation* **51**(10), 2572–2580.
42. **Atallah HA and Hamad EKI** (2010) Radiation pattern improvement of RDRA using LHM flat lens composed of CSRR. *Proceedings of IEEE 1st Middle East Conference on Antennas and Propagation*. Cairo, Egypt.
43. **Pozar DM** (2005) *Microwave Engineering*, 3rd Edn. New York, NY, USA: Wiley.
44. **Jiang HT, Wang ZL, Sun Y, Li YH, Zhang YW, Li HQ and Chen H** (2011) Enhancement of (nearly) homogeneous fields in an (effective) zero-index cavity. *Journal of Applied Physics* **109**(7).
45. **Pendry JB, Holden AJ, Stewart WJ and Youngs I** (2025) Extremely low-frequency plasmons in metallic microstructures, *arXiv preprint*, arXiv:2507.01677.
46. **Smith R, Schultz S, Markoš P and Soukoulis CM** (2002) Determination of effective permittivity and permeability of metamaterials from reflection and transmission coefficients. *Physical Review B* **65**, 195104.
47. **Smith DR, Vier DC, Koschny T and Soukoulis CM** (2005) Electromagnetic parameter retrieval from inhomogeneous metamaterials. *Physical Review E* **71**(3), 036617.
48. **Huang GL, Xu MF, Pang ZY, Li HF, Chen RS, Shao Q and Yang H** (2025) A 0.8-30.5 GHz exponential antipodal Vivaldi antenna with stable radiation for wideband measurement application. *IEEE Antennas and Wireless Propagation Letters* **24**(10), 3350–3354.
49. **Zhang R, Song R, Xin Y, Zu HR and He D** (2025) Ultra-wideband and miniaturized endfire antenna with gain enhancement incorporating SSPPs mode and Vivaldi mode. *IEEE Transactions on Antennas and Propagation* **73**(8), 6091–6096.
50. **Liu B, Zhang Y, Lin J, Zhuo J, Lai K and Ye L** (2024) Endfire gain enhancement enabled by a modified antipodal Vivaldi antenna with metamaterials. *IEEE Photonics Technology Letters* **36**(23), 1385–1388.
51. **Zou Q, Gu Z, Xie R, Zhang Z, Zhang H and Ding J** (2023) High-gain UWB double-slot Vivaldi antenna loaded with metasurface and semi-elliptical slots. *Microwave and Optical Technology Letters* **65**(8), 2412–2417.
52. **Kumar S and Dixit AS** (2024) Enhanced antipodal Vivaldi antenna with SSRR metamaterial for improved 5G performance in the 38 GHz band. *Results in Engineering* **24**, 103133.
53. **Saeidi T, Ismail I, Noghanian S, Alhawari AR, Abbasi QH and Imran MA** (2021) High gain triple-band metamaterial-based antipodal Vivaldi MIMO antenna for 5G communications. *Micromachines* **12**(3), 250.
54. **Paul S, Rana S, Azad AR, Nandi D and Mohan A** (2025) Compact planar UWB microstrip antenna with independently controllable dual notch bands. *ETRI Journal* **47**(6), 1125–1138.
55. **Lai H, Lei ZY, Xie YJ, Ning GL and Yang K** (2011) UWB antenna with dual band rejection for WLAN/WiMAX bands using CSRRs. *Progress in Electromagnetics Research Letters* **26**, 69–78.
56. **Chu QX and Yang YY** (2009) A compact ultrawideband antenna with 3.4/5.5 GHz dual band-notched characteristics. *IEEE Transactions on Antennas and Propagation* **56**(12), 3637–3644.
57. **Zeain MY, Abu M, Althuwayb AA, Alsariera H, Al-Gburi AJA, Abdulbari AA and Zakaria Z** (2024) A new technique of FSS-based novel chair-shaped compact MIMO antenna to enhance the gain for sub-6 GHz 5G applications. *IEEE Access* **12**, 49489–49507.



Manoj Bhaskar was born in Sitamarhi, India, in 1989. He received the B.Tech. degree in Electronics and Communication Engineering from Asansol Engineering College, West Bengal, in 2011, and the M.Tech. degree in Electrical Engineering, specializing in RF, Microwaves, and Photonics, from the Indian Institute of Technology (IIT) Kanpur in 2014. He is currently serving as an Assistant Professor in the Department of Electronics and Communication Engineering at the Government Engineering College, Banka, Bihar, India. With over nine years of academic and teaching experience, he is also currently pursuing a part-time Ph.D. at the Indian Institute of Information Technology (IIIT) Bhagalpur. His primary research interests include antenna design, the development and applications of metamaterials, microwave imaging, and NDT. His work focuses on leveraging EM properties for advanced sensing and wireless communication technologies.



Dr. Chetan Barde was born in Jabalpur, India, in 1986. He received the B.E. degree in Electronics & Communication Engineering from the RGPV University, Bhopal, India, in 2008, and the M.Tech degree in Nanotechnology from the VIT University, Vellore, India, in 2013. He completed Ph.D. from the National Institute of Technology Jamshedpur, India. His research interests include ZOR antenna, metamaterials & its applications, and EM wave absorbers. He joined the Department of Electronic and Communication Engineering, IIIT Bhagalpur, India, as an Assistant Professor and became an Assistant Professor in 2023. His current research interests include signal processing, communication, soft computing, and antenna design.



Dr. Prakash Ranjan was born in Vaishali, India, in 1982. He received the B.E. degree in Electronics & Communication Engineering from Anna University, Chennai, India, in 2009, and the M.Tech. degree in Electronics & Communication Engineering from the YMCA University, Haryana, India, in 2012. In 2019, he completed his Ph.D. at the National Institute of Technology, Jamshedpur, India, and subsequently joined the Department of Electronics & Communication Engineering, Indian Institute of Information Technology, Bhagalpur, as Assistant Professor. He is a graduate student member of IEEE. His research interests include metasurfaces, metamaterials & its applications, EM wave absorbers, ZOR antenna, and soft computing optimization techniques.



Dr. Sujit Kumar is working as the Assistant Professor in the Electrical Engineering Department at Government Engineering College, Banka. He completed his Ph.D. in January 2025 at the National Institute of Technology, Nagaland, 797103, India. He received his Master's degree in the year 2018 from the National Institute of Technology, Uttarakhand, 246174, India. His research interests include the application of artificial intelligence in fault diagnosis.

https://doi.org/10.1017/S1759078726103353 Published online by Cambridge University Press



Himanshu Kumar Shekhar was born in Bhagalpur, India, in 1993. He received the B.Tech. degree in Electronics and Communication Engineering from Punjab Technical University, Jalandhar, India, in 2014, and the M.Tech. degree in Electronics and Communication Engineering from the National Institute of Technology Karnataka (NITK), Surathkal, India, during 2016–2018. He is currently serving as an Assistant Professor in the Department of Electronics and Communication Engineering at Government Engineering College, Banka, Bihar, India. With more than six years of teaching and academic experience, he is presently pursuing a part-time Ph.D. at the Indian Institute of Technology (IIT) Roorkee, Uttarakhand, India. His primary research interests include wireless communication technologies, non-orthogonal multiple access (NOMA), intelligent reflecting surfaces (IRS), and MIMO antenna systems.



Dr. Bam Bahadur Sinha is an Assistant Professor in the Department of Computer Science and Engineering at the National Institute of Technology Sikkim. Prior to this, he was serving as an Assistant Professor at the Indian Institute of Information Technology Ranchi. He received the M.Tech. and Ph.D. degrees in Computer Science & Engineering from the National Institute of Technology Nagaland in 2017 and 2020, respectively. He was awarded a Gold medal in M.Tech. at NIT Nagaland in the year of 2017. His areas of expertise include artificial intelligence, machine learning, deep learning, optimization techniques, and recommender systems.

https://doi.org/10.1017/S1759078726103353 Published online by Cambridge University Press